

A High-Speed Imaging and Modeling Study of Dendrite Fragmentation Caused by Ultrasonic Cavitation

DA SHU, BAODE SUN, JIAWEI MI, and PATRICK S. GRANT

The dynamic behavior of ultrasound-induced cavitation bubbles and their effect on the fragmentation of dendritic grains of a solidifying succinonitrile 1 wt pct camphor organic transparent alloy have been studied experimentally using high-speed digital imaging and complementary numerical analysis of sound wave propagation, cavitation dynamics, and the velocity field in the vicinity of an imploding cavitation bubble. Real-time imaging and analysis revealed that the violent implosion of bubbles created local shock waves that could shatter dendrites nearby into small pieces in a few tens of milliseconds. These catastrophic events were effective in breaking up growing dendritic grains and creating abundant fragmented crystals that may act as embryonic grains; therefore, these events play an important role in grain refinement of metallurgical alloys.

DOI: 10.1007/s11661-012-1188-3

© The Minerals, Metals & Materials Society and ASM International 2012

I. INTRODUCTION

SUBJECTING liquid metallic alloys to an ultrasonic field with a sound intensity above a certain threshold can produce refined, nondendritic microstructures, as shown in Al-,^[1,2] Mg-,^[3,4] and Ni-based alloys and steels.^[5,6] The grain refinement effect can occur when ultrasound is applied to the alloy melt at a temperature above its liquidus temperature or between the liquidus and solidus temperatures during solidification. The links between the resulting grain size of an alloy solidified in this manner and the various ultrasonic parameters, *i.e.*, frequency, intensity, power density, *etc.* applied during solidification, have been studied by postmortem microstructural analysis^[7–9] and have provided some useful experimental correlations.

The proposed mechanisms for grain refinement caused by ultrasound generally fall into three categories: (1) the promotion of homogeneous grain nucleation by increasing the alloy melting point and therefore leading to a melt undercooling at locations immediately adjacent to any imploding ultrasonic cavities or bubbles (when cavities are filled with vapor or gas nucleated in an ultrasonic field with the sound intensity above a certain threshold^[1]) because of the transient high pressure generated during implosion^[10,11]; (2) the enhancement of heterogeneous nucleation by “activating” insoluble impurity particles in the melt, *e.g.*, oxide inclusions, by increasing wettability with the melt,

reducing agglomeration, *etc.*^[1,5]; and (3) the multiplication of grains by fragmentation of growing dendrites to seed the formation of new grains ahead of the solidification front. In reality, one or all of the mechanisms may come into play at different stages of solidification.

Given the potency of the grain refinement effect (up to an order of magnitude) and the potential technological implications for the casting industry, increasing the currently limited mechanistic understanding of ultrasound in liquid and semisolid metals is important. *In situ* observation of dendritic microstructure evolution in real time is likely to be helpful to reveal the relative importance of each ultrasonic parameter at different stages of solidification.

Direct observation of solidification, usually comprising dendritic growth, can be realized by optical imaging of transparent alloys, and this approach has been widely used to investigate the dynamics of dendrite evolution under different thermal regimes, mechanical stirring/shearing conditions, *etc.*, which mimic the conditions often found in the processing of metallic alloys.^[12,13] In the presence of ultrasound or vibration, direct photographic observations^[1,14] of solidifying ammonium chloride solutions have shown that the crystal morphology can be induced to change from branched dendrites to a fine granular grain structure. A photographic study at ~500 frames per second (fps) of a transparent camphene-based alloy solidified in an ultrasonic field^[15] attempted to study the effect of ultrasound cavitation on dendrite fragmentation. Dendrite fragmentation caused by cavitation bubbles has also been reported in the sonocrystallization (crystallization in the presence of an ultrasonic wave) of ice in sucrose solutions at a microscopic scale,^[16,17] where highly mobile cavitation bubbles broke up existing ice dendrites. Although some images presented in these previous studies show fragmented crystals or dendrites, the highly dynamic interaction between bubbles and the growing dendrites was not resolved in sufficient spatial or temporal detail to

DA SHU, Associate Professor, and BAODE SUN, Professor, are with the State Key Laboratory of Metal Matrix Composites, Shanghai Jiao Tong University, Shanghai 200240, P.R. China. Contact e-mail: dshu@sjtu.edu.cn JIAWEI MI, Lecturer and Royal Society Industry Fellow, is with the Department of Engineering, University of Hull, East Yorkshire HU6 7RX, UK. PATRICK S. GRANT, Cookson Professor of Materials, is with the Department of Materials, University of Oxford, Oxford OX1 3PH, UK.

Manuscript submitted September 27, 2011.

Article published online May 16, 2012

gain a clear understanding of the processes producing fragmentation. Consequently, there remains debate on the mechanism of how dendrites are broken up in an ultrasonic field and the contributions of either quasi-steady-state oscillations and flow or highly transient implosions of individual bubbles.

In nondendritic structures, sonocrystallization studies showed that acoustic cavitation can cause the breakage and fracture of single crystals (particulate calcite crystals^[18] or aspirin molecular crystals^[19]). The primary fragmentation mechanism suggested was direct crystal–shock wave interactions. It is well known that the collapse of a bubble emits a shock wave that, in water, has pressures up to 60 kbar and velocity of ~ 4000 m/s.^[20] Cavitation close to a large rigid boundary creates asymmetric bubbles that emit “microjets” toward the boundary when they collapse.^[21] Although both shock waves and microjets are known to cause material erosion, there is no direct evidence for their role in dendrite fragmentation.

Studies of dendrite fragmentation during solidification in the absence of ultrasound have mainly considered dendrite arm remelting effects because of thermal, solute, or capillary effects, as well as mechanical shearing caused by convection flow.^[12,13,22–24] Interdendritic liquid flow velocities are generally low in most casting processes, and therefore, mechanical shearing contributions to fragmentation are suggested to be small.^[12,23] Capillary effects cause dendrite roots to be more soluble than other regions, and disturbances to the solute and thermal field in the liquid surrounding the roots can lead to remelting of the roots and the fragmentation of dendrites.^[12]

In this article, we present images and videos acquired by high-speed digital imaging (up to ~ 8000 fps) of dendritic grain growth of an organic transparent alloy solidified in an ultrasound field, with a focus on the dynamic interplay between the growing dendrites and (1) very fast ultrasonic cavitation of bubbles at a length scale smaller than the primary dendrites and (2) any relatively slow convection flow caused by ultrasonic wave propagation at a length scale larger than the dendrites. The experiments are complemented by a numerical analysis of sound wave propagation and the pressure field near the ultrasonic probe that provides the boundary conditions for an ultrasonic cavitation model that in turn gives the resulting localized velocity field in the melt immediately surrounding an imploding bubble. The data are used semiquantitatively to help understand qualitative observations from experiment. All the models are essentially “standard” and considered valid for the field, with novelty stemming from their application to dendrite fragmentation effects.

II. EXPERIMENTS AND MODELING

A. Experiment

The solidification cell is shown schematically in Figure 1. The cell contains a glass chamber sealed by two copper plates at either side, and it is divided into an upper chamber of dimensions $25 \times 15 \times 4$ mm

(width \times height \times thickness) for accommodating an ultrasonic probe with a thin flat tip of 3×1 mm (width \times thickness) linked to an ultrasound generator and a lower observation chamber of $15 \times 35 \times 1$ mm (width \times height \times thickness). The cell was placed onto an x - y stage composed of two copper blocks through which water of a predefined temperature recirculated from two independently temperature-controlled baths to realize different thermal conditions. A succinonitrile (SCN)-1 wt pct camphor alloy with a liquidus temperature of ~ 328 K (55 °C) was chosen with the thermophysical properties shown in Table I.^[25–27]

The cell that contained the SCN-1wt pct camphor alloy was firstly heated to 353 K (80 °C) in an oven to melt the alloy fully and then placed on the x - y stage. Two thermal configurations were used, as follows:

- (a) The two copper blocks had the same temperature of 343 K (70 °C) to contrive isothermal conditions

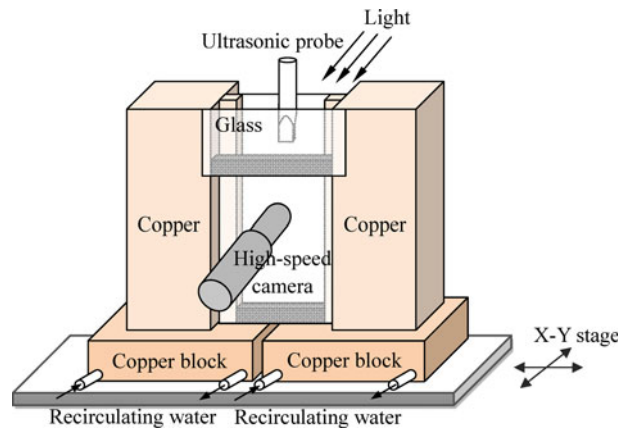


Fig. 1—A schematic view of the experiment setup with a glass chamber containing SCN-1.0 wt pct camphor alloy sitting on top of two independently temperature-controlled copper blocks. A thin, flat ultrasonic probe was immersed into the upper chamber to transmit ultrasound into the melt. The interaction between ultrasonic cavitation bubbles and any growing dendrites was high-speed imaged under the illumination of a tungsten lamp.

Table I. Thermophysical Properties of the SCN-1wt pct Camphor^[25–27] and Other Parameters Used in Calculations

Density of liquid, ρ_0	$0.97 \times 10^3 \text{ kg m}^{-3}$
Viscosity of liquid, μ	$2.66 \times 10^{-3} \text{ Pa s}$
Surface tension, σ	$3.85 \times 10^{-2} \text{ N m}^{-1}$
Thermal diffusivity, D	$0.116 \times 10^{-6} \text{ m}^2 \text{ s}^{-1}$
Ambient sound speed in liquid, c_0	$1450 \text{ m s}^{-1\text{a}}$
Speed of sound in glass, c^*	2380 m s^{-1}
Density of glass, ρ^*	$2.3 \times 10^3 \text{ kg m}^{-3}$
Frequency of ultrasound, f	20 kHz
Ultrasound power, W	50 W
Area of sonotrode tip, A	$3 \times 10^{-6} \text{ m}^2$
Empirical constant, B	$3000 \text{ atm}^{\text{b}}$
Empirical constant, n	7^{c}
Gas polytropic exponent, γ	1.6 (for air)

^{a,b,c}For lack of data for molten SCN, the values of c_0 , B , and n for water are listed in the table and used in calculations.

in the transparent alloy after which the ultrasonic probe at room temperature was introduced into the melt in the upper chamber to a depth of ~10 mm. This process caused solid dendrites to nucleate at the ultrasonic probe tip and then grow downward into the melt, against the direction of heat flow into the relatively cold ultrasonic probe. When the dendrites grew into a field of view of the camera, focus was obtained and high-speed images recorded during which an ultrasound wave of constant amplitude of ~4 μm , a frequency of 20 kHz and a power output of ~50 W was transmitted into the melt via the ultrasonic probe.

- (b) The temperatures of the left- and right-hand side copper blocks were controlled at 333 K to 313 K (60 °C and 40 °C), respectively, allowing dendrites to nucleate on the right-hand side and grow near horizontally from right to left in Figure 1 before ultrasound was applied to the melt in the upper chamber and transmitted through the liquid into the lower chamber.

A Phantom V4.2 (Vision Research, Inc., Wayne, NJ) high-speed digital video camera attached to an optical microscope (~800 times magnification) was used to image the dynamic interaction between the dendrites and the ultrasonic field/cavitation during solidification. The image acquisition rates were 8113 fps at a resolution of 256 \times 256 dots per inch (dpi) or 2252 fps at 512 \times 512 dpi with an optimized exposure time of 90 or 200 μs , respectively, to give the best combination of large view field, image resolution, and contrast.

B. Modeling

1. Acoustic pressure field

Under a time harmonic assumption and by ignoring the effect of cavitation flow, sound waves propagating in a liquid are governed by the Helmholtz equation for the acoustic pressure p_a according to^[28]

$$\frac{\kappa^2}{\rho_0} p_a + \nabla \cdot \left(\frac{1}{\rho_0} \nabla p_a \right) = 0 \quad [1]$$

where ρ_0 refers to the liquid density, κ is the wave number defined as $\kappa = \omega/c_0$, $\omega = 2\pi f$ is the angular frequency, f is the frequency of the sound wave, and c_0 is the speed of sound in the liquid.

Equation [1] was solved for the glass chamber geometry in Figure 1 using the finite element commercial software COMSOL Multiphysics (COMSOL, Inc., Burlington, MA). The boundary conditions were: (1) a pressure source $p_a = p_A \cos(\omega t)$ at the ultrasonic probe tip surface and zero normal derivative of the pressure $\partial p_a / \partial n = 0$ at the side boundaries of the probe (hard boundaries), where $p_A = \sqrt{2\rho_0 c_0 W/A}$ is the amplitude of the imposed ultrasound wave determined by the ultrasound power W and the area of probe tip A ; (2) sound soft boundaries ($p_a = 0$) at the liquid/air interface; and (3) hard boundaries for copper walls and acoustic impedance $Z = \rho^* c^*$ for relatively “soft” glass boundaries, where ρ^* and c^* are the density and sound

velocity of the glass, respectively. Additional parameters used in the calculations are listed in Table I.

2. Ultrasonic cavitation dynamics

The classic Gilmore model^[29] and the Tait equation of state for a liquid were adopted to calculate (1) the evolution of the radius of a spherical cavitation bubble and (2) the pressure and velocity in the liquid at the bubble wall during implosion to analyze the response of a single cavitation bubble to different local acoustic pressures (p_a) provided by the acoustic pressure model previously. Note there was no nucleation step for the cavitation bubble that was assumed to be present in the liquid with an assumed radius based on the experiment (see Section IIIB). The set of equations that must be solved are as follows:

$$R \frac{dU}{dt} \left(1 - \frac{U}{C} \right) + \frac{3}{2} U^2 \left(1 - \frac{U}{3C} \right) = H \left(1 + \frac{U}{C} \right) + \frac{RU}{C} \frac{dH}{dR} \left(1 - \frac{U}{C} \right) \quad (2)$$

$$C^2 = \frac{n(P+B)}{\rho_0} \left(\frac{P+B}{p_0+B} \right)^{-1/n} \quad [3]$$

$$H = \frac{n}{n-1} \frac{(p_0+B)^{1/n}}{\rho_0} \left[(P+B)^{n-1/n} - (p_\infty+B)^{n-1/n} \right] \quad [4]$$

where R , U , P , H , and C denote the radius, velocity, pressure, enthalpy, and speed of sound at the bubble wall, respectively; $p_\infty = p_0 + p_a$ is the pressure at an infinite distance from the cavitation bubble center, and p_0 is the ambient pressure in the liquid. B and n are empirical constants that depend on the particular liquid under consideration (Table I). Assuming any cavity was filled with an ideal gas (air) and obeying the polytropic law, P is given as follows:

$$P(R) = \left(p_0 + \frac{2\sigma}{R_0} \right) \left(\frac{R_0}{R} \right)^{3\gamma} - \frac{2\sigma}{R} - \frac{4\mu U}{R} \quad [5]$$

where R_0 is the initial cavitation bubble radius, σ is the surface tension of the liquid, and μ and γ are the liquid viscosity and the gas polytropic exponent, respectively.

3. Velocity field in the vicinity of an imploding cavitation bubble

The localized velocity field in the region immediately surrounding an imploding cavitation bubble was calculated using another “standard” approach, which is termed the method of characteristics^[30] based on the Kirkwood-Bethe hypothesis: An invariant quantity Y defined as $r(h + u^2/2)$ propagates along outgoing (from the bubble center) “characteristic” curves with the characteristic velocity $c + u$, where r is the radial distance relative to the bubble center, and h , c , and u denote the local enthalpy, velocity, and speed of sound in the liquid, respectively. The velocity and the pressure

field inside the liquid are calculated by integrating their time derivatives along the characteristic curves using the solution from the previously described Gilmore model as initial values. The direction of the characteristic curves as well as the velocity u and the pressure p along these curves are calculated using^[31,32]

$$\frac{dr}{dt} = c + u \quad [6]$$

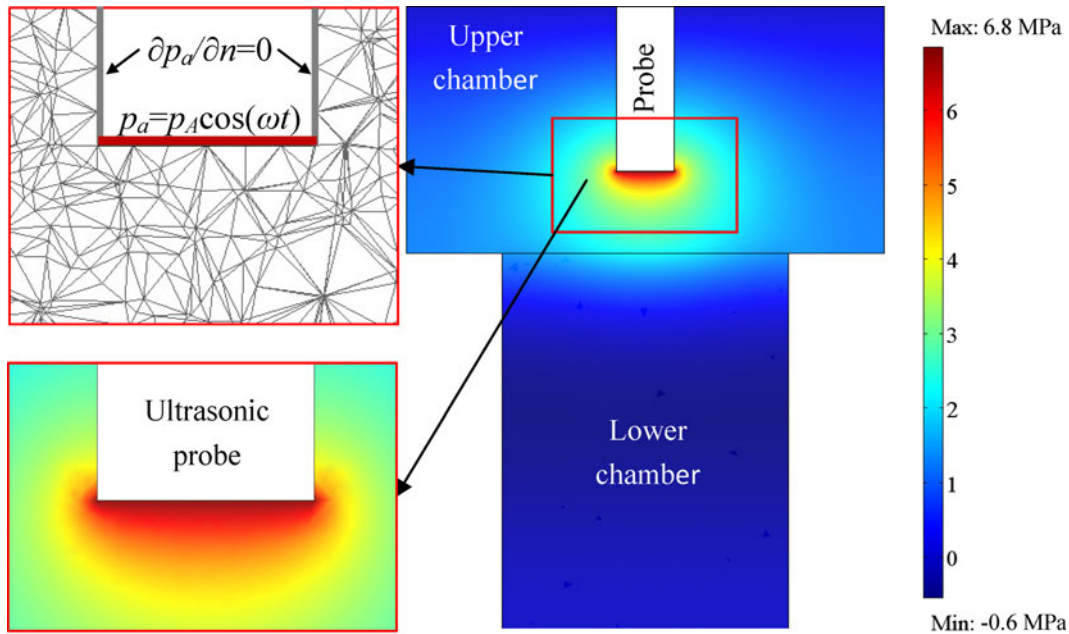
$$\frac{du}{dt} = \frac{1}{r(c-u)} \left[(c+u) \frac{Y}{r} - 2c^2u \right] \quad [7]$$

$$\frac{dp}{dt} = \frac{n(p+B)}{rc(c-u)} \left(2cu^2 - \frac{c+u}{r} Y \right) \quad [8]$$

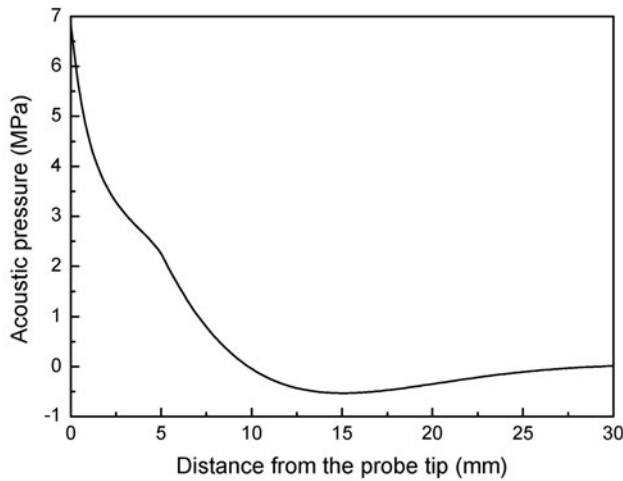
III. RESULTS AND DISCUSSION

A. Acoustic Pressure Distribution

Figure 2(a) shows the calculated instantaneous acoustic pressure field for the SCN-1 wt pct camphor alloy in a two-dimensional plane that includes the ultrasonic probe axis at $t = 0$ (when the highest magnitude of the



(a)



(b)

Fig. 2—The calculated acoustic pressure distribution in the melt at $t = 0$: (a) in the plane of symmetry and (b) along the centerline below the ultrasonic probe tip.

cosinusoidal pressure source is applied in the probe tip), which actually reflects the local peak pressure in the liquid, and thus, the time-varying pressure fluctuates between positive and negative values. A comparatively high acoustic pressure was concentrated in the area around the probe tip. Figure 2(b) shows the calculated pressure variation along the ultrasonic probe axis from the probe tip downward. The acoustic pressure decreased from a maximum of ~ 7 MPa at the tip (antinode) to zero (node) at a distance of ~ 10 mm into the melt. There was a minimum pressure of -0.6 MPa at a distance of ~ 15 mm before the pressure increased gradually to zero again at ~ 30 mm away from the tip. Broadly, the pressure decreased with distance from the tip as the energy was dissipated into the melt and at the relatively “soft” glass boundaries.

B. Quasi-Steady and Chaotic Cavitation

Figure 3 shows three typical images extracted from a high-speed video frames, showing the collective

behavior of many ultrasound cavitation bubbles in the melt (above the liquidus temperature) at different locations relative to the ultrasonic probe tip, including (1) immediately below the tip, either in contact with the tip (zone A in Figure 3(b)) or <1 mm below (zone B in Figure 3(b)), and (2) at a distance of ~ 15 mm below the tip (zone C in Figure 3(c)).

Figure 3(a) shows the region immediately below the ultrasonic probe tip at the point of maximum negative pressure (expansion). There was a dense cloud of ultrasonic cavitation bubbles that grew larger as each individual bubble expanded. Figure 3(b) shows the instant of maximum positive pressure (compression), where bubbles that exceeded a critical size have imploded^[21] (chaotic cavitation), creating a larger number of unstable, smaller diameter bubbles, which then oscillated in the cyclic pressure field. Where these bubbles touched each other, bubbles then usually coalesced to form larger bubbles. Subsequently, these bubbles drifted away from the tip into a lower acoustic pressure region because of both a hydrodynamic (drag)

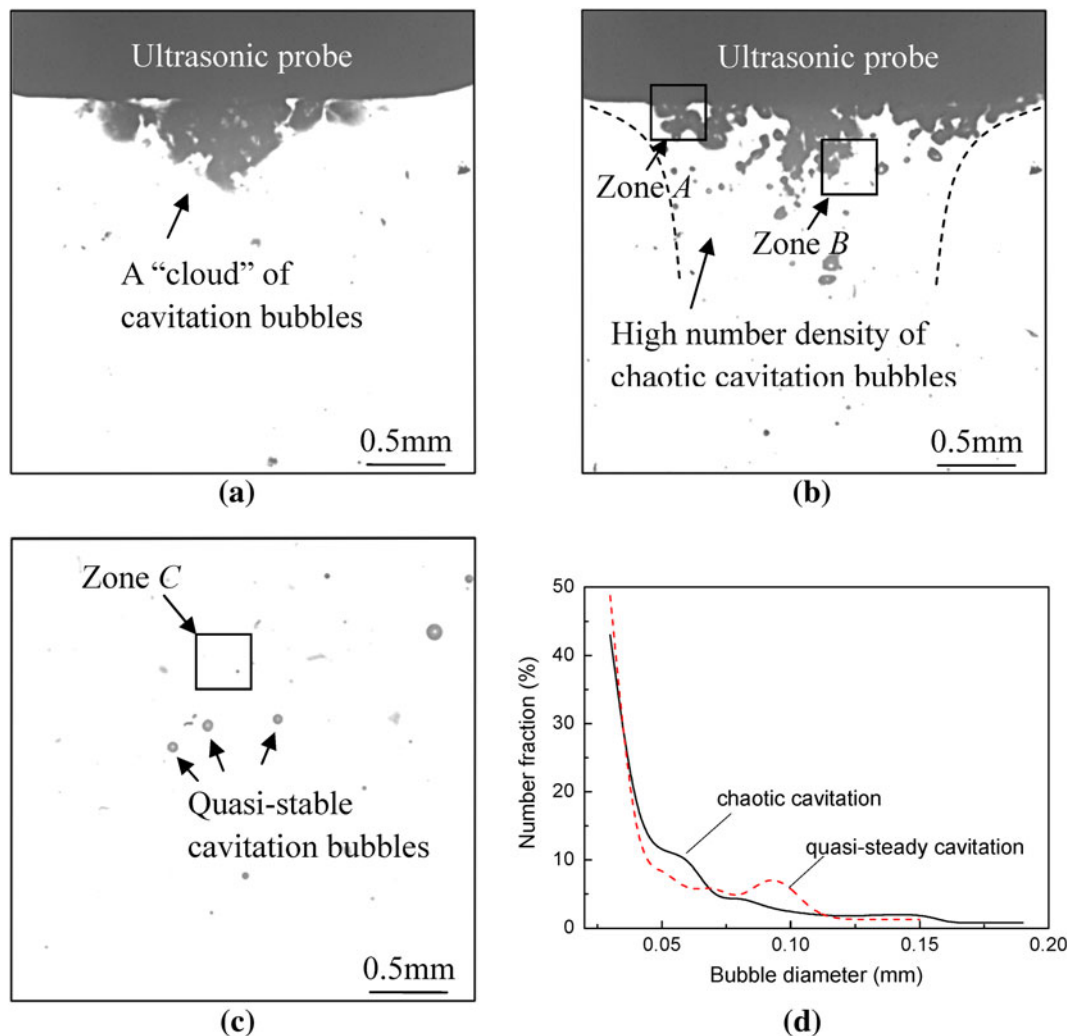


Fig. 3—High-speed image frames extracted from digital video, showing chaotic cavitation and regions immediately below the ultrasonic probe in (a) a negative (expansion) half period of the wave and (b) a positive (compression) half period of the wave. (c) The quasi-steady cavitation bubbles and region at ~ 15 mm below the probe tip. (d) The measured bubble size distributions over ~ 200 cavitation events. (Cavitation bubbles appear dark as they scatter away the illuminating back-light. Zones A, B, and C were the regions where subsequent *in situ* imaging studies of solidification were focused.).

force and the acoustic pressure gradient force (known as the Bjerknes force in a sound field). These bubbles continued to oscillate in the streaming flow but with a smaller amplitude because the chaotic implosion at the region near the ultrasonic probe tip consumed much of the ultrasonic energy and therefore, are termed “quasi-steady” cavitation (Figure 3(c)).

A normalized distribution of bubble diameter in the range 0.02 to 0.2 mm based on ~200 chaotic and quasi-steady cavitation events selected by eye from many image frames is shown in Figure 3(d). Generally, the number of bubbles decreased rapidly with increasing bubble diameter. A slight increase in the number fraction of bubble diameters of ~0.1 mm for the quasi-steady cavitation bubbles indicated that coalescence of smaller cavitation bubbles may occur. There may be a significant population of bubbles below the resolution of the imaging arrangement (<0.02 mm).

C. Implosion of Cavitation Bubbles at Different Acoustic Pressures

The change in radius, pressure, and velocity of the bubble/liquid boundary for individual bubbles of initial radius of 0.1 mm (starting at an ambient pressure) were calculated by applying acoustic pressures of $p_a = 6$ MPa or 0.6 MPa, respectively, representing typical near maximum pressure calculated for zone B in Figure 3(b) and zone C in Figure 3(c).

Figure 4(a) shows that in the case of $p_a = 0.6$ MPa, the cavitation bubble was restricted to a compression of less than half the initial radius in ~4 μ s before expanding (rebounding) gradually back to the original size. In the case of $p_a = 6$ MPa much nearer to the ultrasonic probe, the cavitation bubble collapsed to approximately one fifth of the initial radius in ~1.2 μ s, and then it experienced a series of nonlinear compression/expansion cycles characterizing chaotic cavitation implosion. Figures 4(b) and (c) show that initially during collapse at 6 MPa, the pressure at the bubble wall increased abruptly and sharply to a peak value of ~400 MPa when minimum radius was reached, resulting in an abrupt reversal of boundary velocity from ~300 m/s inward during collapse to ~200 m/s outward during rebound and the release of pressure. The time for this velocity reversal was a few tens of nanoseconds, and in practice, it results in a high energetic shock wave emanating outward from the cavitation bubble and microjet flow if the bubble is close to a solid surface. This phenomenon is commonly found in sonication processes.^[21] Subsequently, the pressure and velocity magnitudes were damped progressively in a series of compression/rebounding cycles, with peak magnitudes decreasing quickly. In contrast, the peak pressure and velocity calculated for a field pressure of 0.6 MPa reached just ~5 MPa and ~27 m/s, respectively, followed by a much slower rebounding cycle, which qualitatively explains the observation of quasi-steady cavitation bubbles in zone C in Figure 3(c).

Figures 5(a) and (b) show the calculated liquid velocity as a function of the distance from the bubble center at different times immediately after rebounding

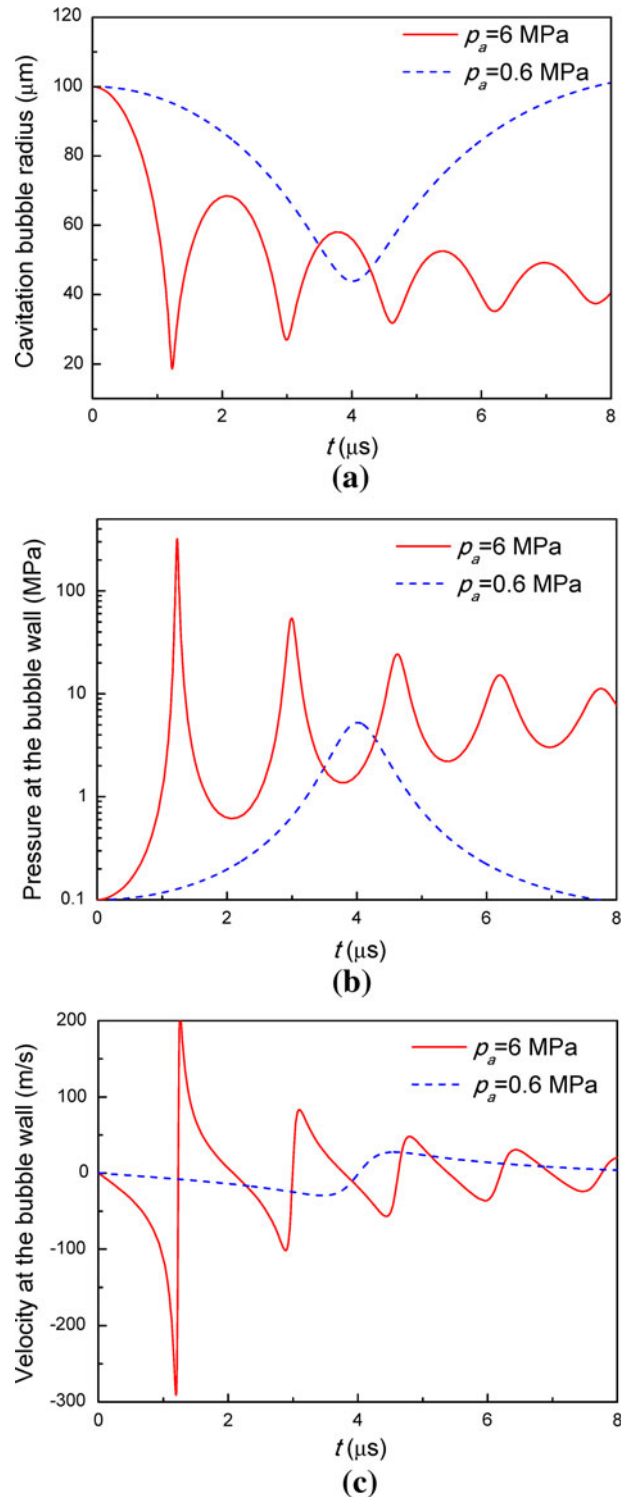


Fig. 4—The calculated (a) cavitation bubble radius, (b) pressure, and (c) velocity at the bubble wall during implosion and subsequent rebounding stages (the initial bubble radius is 0.1 mm).

from the minimum radius for chaotic and quasi-steady cavitation, respectively. In both cases, the liquid velocity decreased exponentially with distance from the peak velocity. Figure 5(a) shows that the quasi-steady cavitation velocity at the boundary reached its maximum of

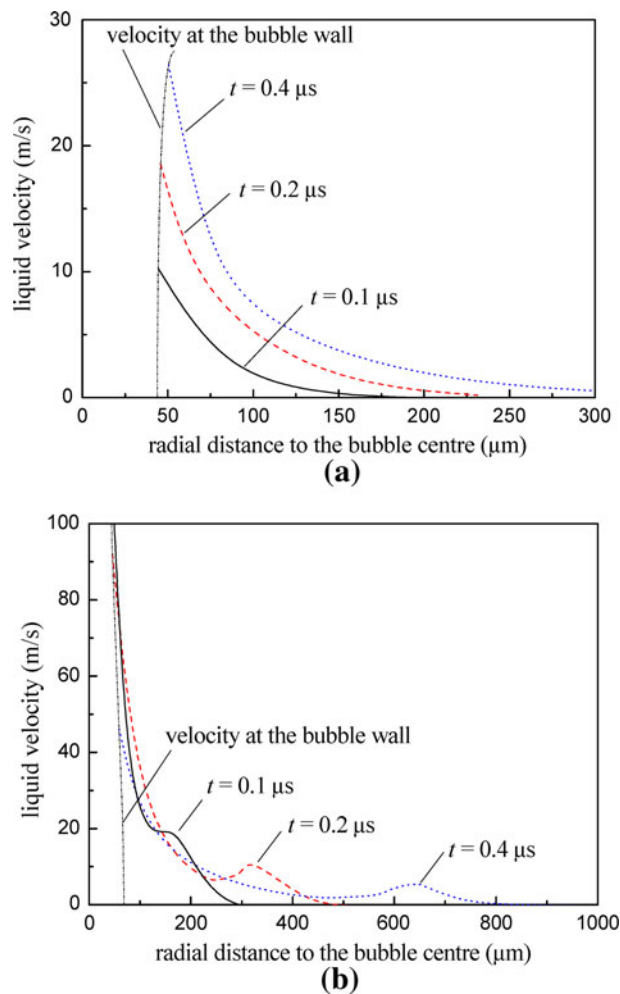


Fig. 5—The velocity profiles in the liquid at the vicinity of the cavitation bubble at different times immediately after the implosion (the minimum bubble radius) for (a) quasi-steady cavitation and (b) chaotic cavitation.

27 m/s within $0.4 \mu\text{s}$ after rebounding, and the liquid velocity at a distance $>0.3 \text{ mm}$ away from the bubble center was $<1 \text{ m/s}$. Figure 5(b) shows that for chaotic cavitation, the velocity reached its maximum after a few tens of nanoseconds and then propagated outward as shock waves. Although the velocity magnitude was damped exponentially, it was maintained at $10 \pm 3 \text{ m/s}$ for as long as $\sim 0.4 \mu\text{s}$ within regions up to $\sim 0.6 \text{ mm}$ away from the bubble center.

D. Interactions Between Cavitation Bubbles and Dendrites

1. Effect of chaotic cavitation

Figure 6 shows three near-parallel dendrites nucleated on the relatively cold ultrasonic probe tip that grew approximately in a downward direction into the melt. Immediately after applying ultrasound, a single bubble became apparent in the melt, probably nucleating on a gas pore or impurities just below the dendrite tips, which then traveled rapidly toward the ultrasonic probe tip where it collided into a growing dendrite. Individual

image frames were extracted from the video to highlight the motion of the bubble and its dendrite interaction. Figure 6(a) shows the instant when the bubble touched the dendrite tip. As the bubble moved upward in the direction indicated by the arrow in each subsequent image, the dendrite primary arm started to bend and a few secondary dendrite arms were detached progressively from the main trunk as shown in Figures 6(b) through (e), until an outward shock wave caused by the expansion of bubble wall completely broke away secondary arms from the main trunk, as shown in Figure 6(f). The shock wave was characterized by a sudden halo of blurred, darker contrast around the bubble, and it was remarked many times.

During the exposure time of $200 \mu\text{s}$ for each individual image, the bubble was estimated to be subject to ~ 4 cycles of expansion and compression, and therefore, the image acquisition rate was not high enough to resolve fully the details of bubble implosion. However, the sudden appearance of many dendrite fragments in images after an apparent bubble implosion suggested that fragmentation of secondary dendrite arms occurred over a time scale much shorter than the interval of image acquisition of 0.44 ms .

Figure 7 shows another case where a detached dendrite from the ultrasound probe tip interacted with a chaotic cavitation bubble, and the primary dendrite “trunk” was first bent and then fractured between two consecutive image frames (0.44 ms).

In general, the high-speed images showed that after touching the dendrites, cavitation bubbles could markedly and violently bend both primary and secondary arms, leading to the detachment of secondary arms (Figure 6(e)) at the root or even fracture of the primary trunk (Figure 7(b)).

2. Effect of quasi-steady cavitation

Figure 8 shows a quasi-steady cavitation bubble of a diameter $\sim 0.2 \text{ mm}$ oscillating or “pulsing” at a primary dendrite tip of the type typically observed in zone C in Figure 3(b). In this case, the second experimental arrangement was employed where there was a temperature gradient of $\sim 0.6 \text{ K/mm}$ from left to right that allowed a relatively large dendrite to grow into the field of view from right to left. The quasi-steady cavitation bubble was pushed gently downward by the propagation of ultrasonic waves from the ultrasonic probe (out of sight), until the bubble just contacted the dendrite tip (Figure 8(a)). The bubble expanded and contracted periodically at the frequency of the imposed ultrasound. First, it created a “cleavage” at a secondary dendrite arm after 232 wave periods (11.59 ms) as indicated by the arrow in Figure 8(b), and then as bending continued, the cleavage developed into partial fracture (Figure 8(c)) and, finally, to failure that broke the dendrite side-arm from the trunk (Figure 8(d)). This sequence occurred over 315 wave periods, equivalent to 15.77 ms .

After a careful analysis of the many such images from the experiment, it was concluded that the fragmentation of growing dendrites caused by ultrasonic cavitation occurred within a distance of a few tens to hundreds of

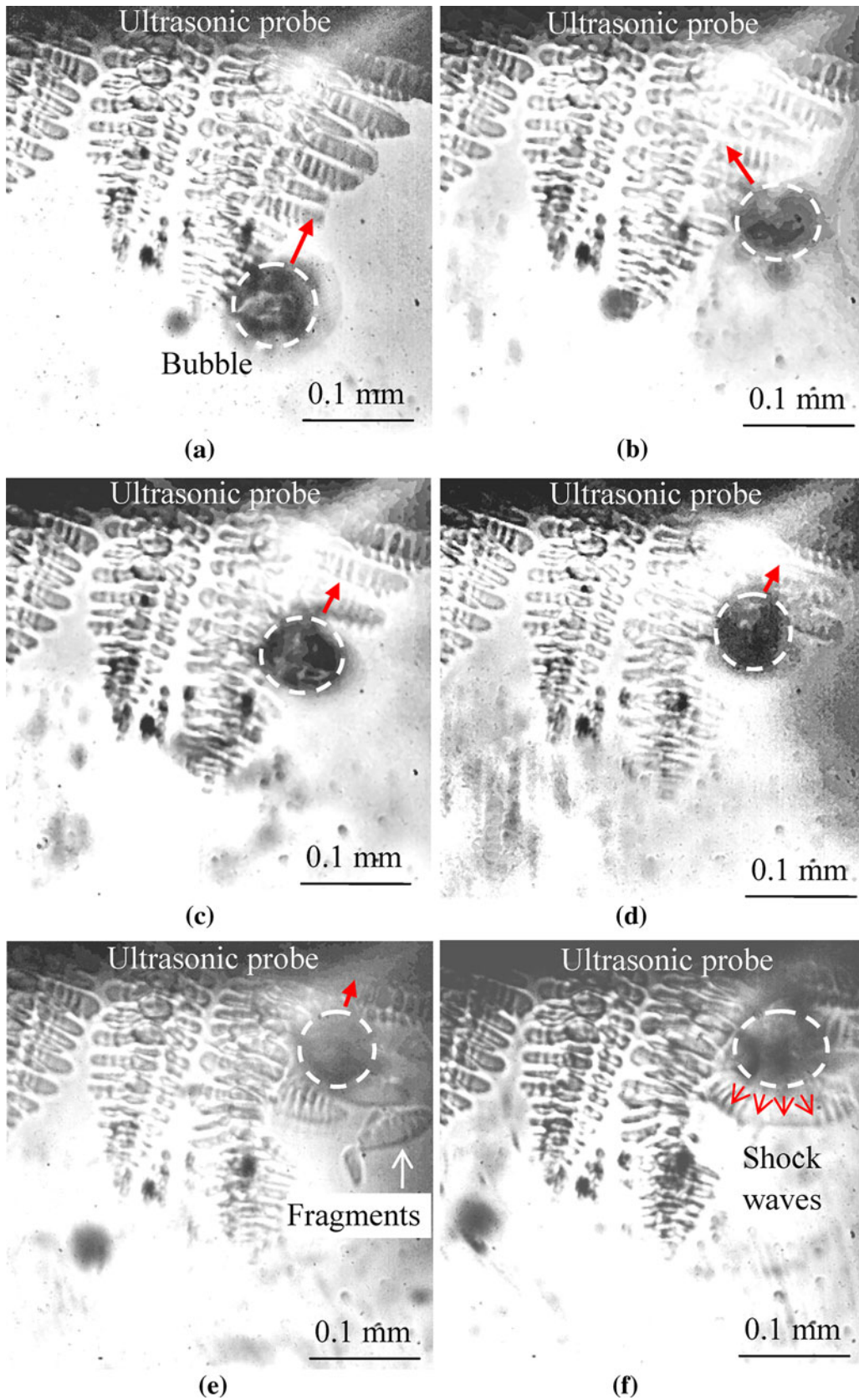


Fig. 6—A series of high-speed imaging frames, detailing the interactions between a chaotic, traveling cavitation bubble (circled by dashed lines and the arrows pointing to the direction of move) and a dendrite: (a) direct contact with dendrite arms; (b) through (e) bending and fracturing of dendrite arms; and (f) emitting shock waves during implosion. The image acquisition rate is 2252 fps, equivalent to an interval of 0.44 ms or 8.8 wave periods between two consecutive frames.

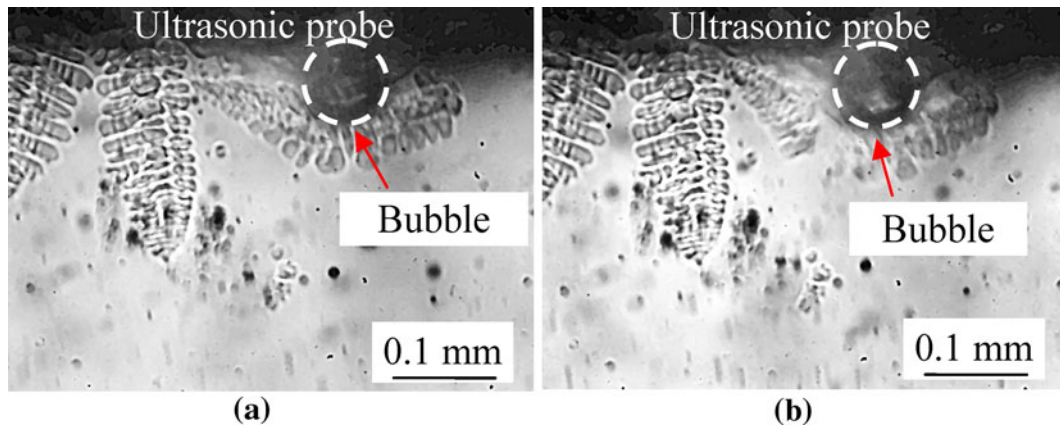


Fig. 7—Fragmentation occurred at the primary dendrite stem: (a) before fragmentation and (b) after fragmentation (within a time interval of 0.44 ms).

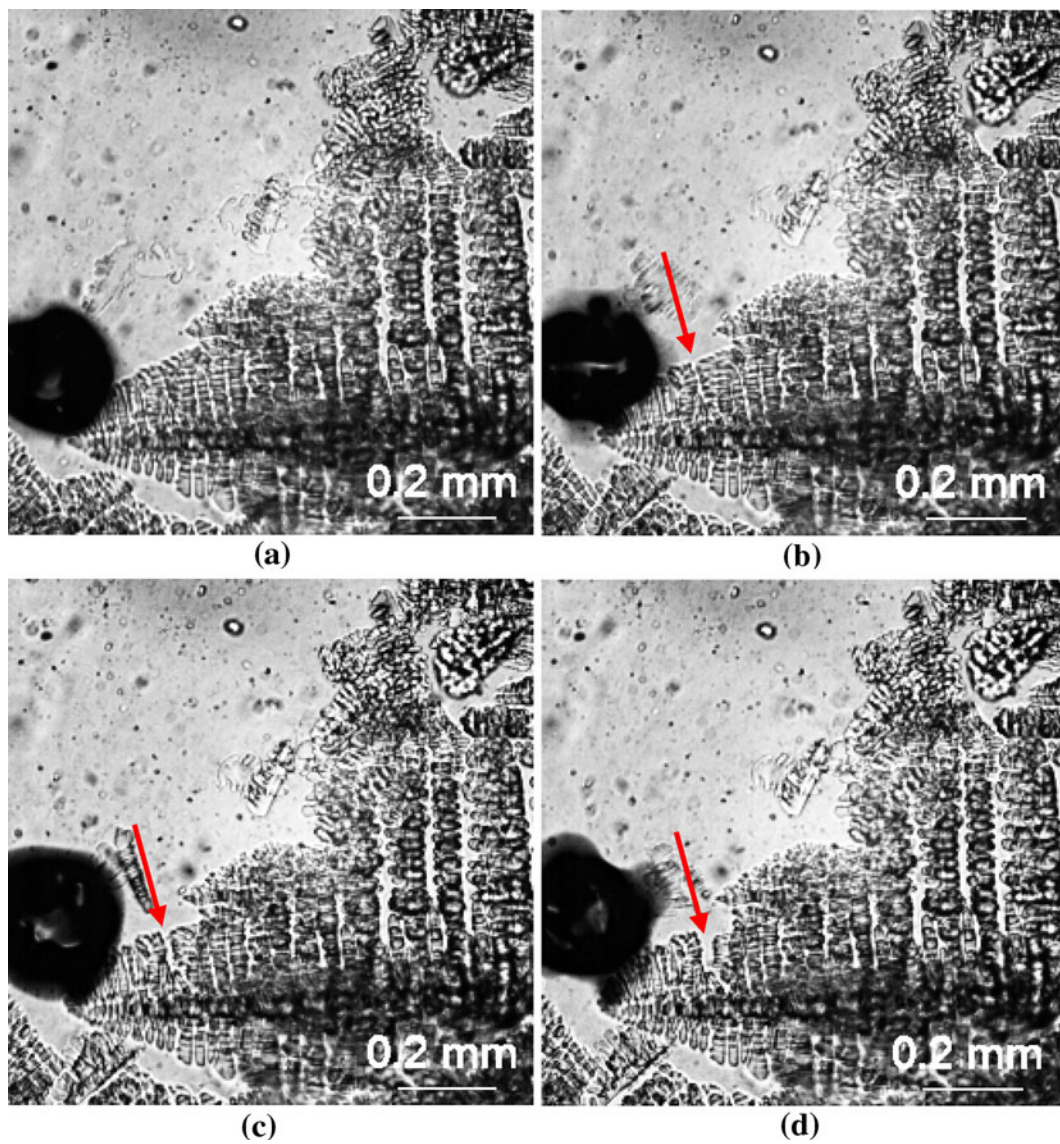


Fig. 8—The process of fracturing a secondary dendrite arm by a quasi-steady cavitation bubble pulsing on the tip of a dendrite at (a) $t = 0$, the start; (b) $t = 11.59$ ms, after wave 232 periods; (c) $t = 13.93$ ms, after 279 periods; and (d) $t = 15.77$ ms, after 315 periods. The images were recorded at 8113 fps.

micrometers around a cavitation bubble, but fragmentation was much more effective when the cavitation bubbles almost touched dendrites, at which point the fragmentation progressed quickly over a single or few video frames (perhaps only few tens of nanoseconds) for chaotic cavitation, or less effectively over a few tens of milliseconds for quasi-steady cavitation.

The observations in the current work are made necessarily in a small volume of an organic transparent alloy solidified in ultrasonic field, whereas most castings of industrially important metals are measured in centimeters or meters. Despite this scale difference, ultrasound is effective in grain refinement in the larger castings (see Section I), and the relevance to the current work is that the results in this article suggest that even in larger castings, the zone of effective dendrite break up as a result of ultrasound will always be quite restricted and confined only to those regions where unsteady cavitation bubbles interact directly with the growing dendrite front. The density of the organic alloy in this article was close to that of water, and whereas light alloys based on Mg and Al may show qualitatively similar behavior, ferrous and other denser alloys are likely to require considerably more energetic ultrasonic excitation to produce similar scale effects (for example, see Eq. [1]).

E. Effect of Ultrasound-Induced Streaming Flow

Considerable bulk streaming flow was induced by the ultrasound and was effective in transporting dendrite fragments away from the dendrite front, but we found no compelling evidence that under the conditions studied in this article, this larger scale flow contributed to any fragmentation behavior directly. In the absence of cavitation bubbles, the dendrites proved extremely robust to any flow perturbation. However, streaming flow still plays an important role in ultrasound treatment because it continuously projects entrained chaotic cavitation bubbles at the dendrite front. By measuring the displacement of the same fragments over several acquired images, the magnitude of the macroscopic streaming flow velocity was estimated as a few tens of millimeters per second. Without this induced macroscopic flow, the region of interaction between bubbles and dendrites would be much smaller and fragmentation effects, consequently, much reduced.

F. The Mechanism of Dendrite Fragmentation by Imploding Cavitation Bubbles

As mentioned, fragmentation mechanisms may include dendrite root remelting as a result of thermal, solute, or capillary effects as well as mechanical break up. It is well known that the gases and vapors inside bubbles are highly compressed during the rapid, nearly adiabatic implosion of a bubble, potentially generating intense heat that may raise the temperature of the liquid immediately surrounding the bubble. In the case of chaotic cavitation of the type shown in Figure 4 and assuming adiabatic heating, the temperature inside the bubble can be roughly estimated to reach ~ 6000 K (5727 °C) at the minimum radius of ~ 20 μm over a time

of $\sim 10^{-7}$ seconds. However, the remelting of dendrite roots as a result of this local heating effect is suggested unlikely under the conditions studied because although the temperature at the bubble wall may be very high, the resulting temperature increase in nearby liquid through radiation or conduction is estimated to be negligible.^[10] For example, if a bubble of radius 20 μm radiates like a black body at 6000 K (5727 °C) and all the energy emitted in 10^{-7} seconds is absorbed by a thin “shell” of liquid with an outer radius of 30 μm enveloping the bubble, the average temperature rise is only a few tenths of degrees. Similarly, an increase in temperature because of conduction is also negligible because the thermal diffusion length l ($= 2\sqrt{Dt}$) in the liquid is estimated to be only a few tenths of a micron.

For most chaotic bubble cavitation cases, dendrites that fragmented did so at or very close to their secondary dendrite roots over a short period of time. Not all cavitation bubbles produced dendrite fragmentation, usually when dendrites were typically an order of magnitude or larger than the cavitation bubbles, presumably as forces were distributed over a large root area.

To gain an estimate of the mechanical force because of the localized melt flow associated with imploding cavitation bubbles, we adopt the model proposed by Pilling and Hellawell^[33] to analyze the instantaneous stress acting on a dendrite arm resulting from the convective flow perpendicular to the arm. Figure 9 shows a schematic view of the assumed geometry, with both the dendrite root and the secondary arm assumed to be cylindrical with diameters d_r and d and length L , respectively. The stress σ acting on the arm because of an interdendritic flow velocity field can be estimated by^[33]

$$\sigma(x) = \frac{-M(x)r(x)}{I(r(x))} \quad [9]$$

$$M(x) = \frac{-Fx^2}{2} \quad [10]$$

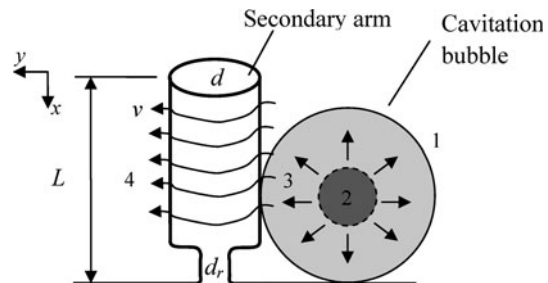


Fig. 9—A schematic view showing the interaction between a secondary dendrite arm and an ultrasonic cavitation bubble: (1) the bubble touches upon a dendrite; (2) the bubble implodes to its minimum radius; (3) the bubble rebounds and expands; and (4) creating flow velocity field perpendicular to the secondary arm, causing stress concentration at the root.

$$I(r(x)) = \frac{\pi(r(x))^4}{4} \quad [11]$$

where M is the bending moment, I is the moment of inertia of the section, r is the radius of the section, and $F = 3\pi\mu v$ is the force per unit length acting on the dendrite arm perpendicularly.

Based on the measurement of dendrites in captured images, L is in the range of 10 to 500 μm and d varies from 10 to 50 μm . Using Eqs. [9] through [11], the stress at the root of the arm with $d_r = 10 \mu\text{m}$ and $L = 100 \mu\text{m}$ is estimated at 1.28 MPa and 12.8 MPa for $v = 1 \text{ m/s}$ and 10 m/s , representing the typical liquid velocities previously calculated for a quasi-steady cavitation bubble and an imploding chaotic cavitation bubble, respectively. Although there is a lack of accurate measurement or reliable information about the strength of the SCN-1wt pct camphor in this semisolid temperature range, it is likely that the strength of SCN-1 wt pct camphor is less than 1MPa, based on a yield strength of Al at its melting point of $\sim 6.5 \text{ MPa}$.^[33] Therefore, the stress at a dendrite root caused by the close proximity of cavitation is of the correct magnitude to exceed the dendrite strength, and despite the likely very significant plasticity at this temperature, fracture results because the sudden and very fast application of stress exceeds the ability of the material to accommodate the associated strain by large scale dislocation motion. Such failure may easily occur by simple sliding off of the secondary arm on a single slip plane activated by a shear stress.

This mechanism considers only mechanical fracture at dendrite roots induced by a very close imploding bubble. However, other failure mechanisms may also operate. For example, Vogel *et al.*^[34] suggest that dendrites may bend rather than fracture when exposed to turbulent fluid flow, leading to the formation of a high-angle grain boundary by recovery and recrystallization processes, followed by liquid attack at the grain boundary, and finally the separation of the dendrite arm from the dendrite by grain-boundary-induced melting. We cannot provide conclusive proof of a single mechanism, but in the case of ultrasound-induced fracture because of the bubble collapse, any mechanism must operate at a very high speed.

IV. CONCLUSIONS

Dendrite fragmentation in a transparent low-melting-point alloy caused by ultrasonic cavitation bubbles has been studied using high speed digital imaging and the insights gained have been supported by numerical modeling of pressure wave propagation and cavitation bubble dynamics. Both chaotic cavitation and quasi-steady cavitation could cause dendrite fragmentation in regions typically less than a few hundreds of micrometers from the cavitation bubble, in a time-scale spanning a few milliseconds, but chaotic bubble cavitation was much more effective in producing fragmentation of secondary dendrites. Primarily because of the speed of

fragmentation, it has been suggested that the stress generated by the highly localized convective flow caused by the cavitation bubble collapse imparted sufficient force to fracture dendrite roots, and this idea was supported by a simple estimate of the dendrite root stress as a result of convection. The ultrasound-induced streaming flow played no direct role in the fragmentation of dendrites but was effective in transporting cavitation bubbles toward the dendrite array to promote continuous fragmentation of the growing dendrites.

ACKNOWLEDGMENTS

The authors would like to thank the financial support from the National Natural Science Foundation of China (Nos. 50825401 and 51174135), the National Basic Research Program of China (No. 2012CB619505), the U.K. Royal Society (International Joint Project 2007/R4, Research Grants 2010 R2 and an Industry Fellowship award), and the U.K. Engineering and Physical Sciences Research Council Centre for Liquid Metal Engineering (Grant No. EP/H026177/1).

ELECTRONIC SUPPLEMENTARY MATERIAL

The online version of this article (doi:[10.1007/s11661-012-1188-3](https://doi.org/10.1007/s11661-012-1188-3)) contains supplementary material, which is available to authorized users.

REFERENCES

1. G.I. Eskin: *Ultrasonic Treatment of Light Alloy Melts*, 1st ed., Gordon and Breach Science Publishers, Amsterdam, the Netherlands, 1998.
2. X. Jian, H. Xu, T.T. Meek, and Q. Han: *Mater. Lett.*, 2005, vol. 59, pp. 190–93.
3. X. Liu, Y. Osawa, S. Takamori, and T. Mukai: *Mater. Sci. Eng. A*, 2008, vol. 487, pp. 120–23.
4. D. Gao, Z. Li, Q. Han, and Q. Zhai: *Mater. Sci. Eng. A*, 2009, vol. 502, pp. 2–5.
5. O.V. Abramov: *Ultrasonics*, 1987, vol. 25, pp. 73–82.
6. Q. Liu, Q. Zhai, F. Qi, and Y. Zhang: *Mater. Lett.*, 2007, vol. 61, pp. 2422–25.
7. T.V. Atamanenko, D.G. Eskin, L. Zhang, and L. Katgerman: *Metall. Mater. Trans. A*, 2010, vol. 41A, pp. 2056–66.
8. M. Qian and A. Ramirez: *J. Appl. Phys.*, 2009, vol. 105, pp. 013538.1–013538.6.
9. G.I. Eskin: *Metallurgist*, 2003, vol. 47, pp. 265–72.
10. R. Hickling: *Nature*, 1965, vol. 206, pp. 915–17.
11. J.D. Hunt and K.A. Jackson: *J. Appl. Phys.*, 1966, vol. 37, pp. 254–57.
12. C.J. Paradies, R.N. Smith, and M.E. Glicksman: *Metall. Mater. Trans. A*, 1997, vol. 28A, pp. 875–83.
13. T. Li, X. Lin, and W. Huang: *Acta Mater.*, 2006, vol. 54, pp. 4815–24.
14. W.L. Wang, K.S. Wang, and X. Lin: *Int. J. Cast Met. Res.*, 2010, vol. 23, pp. 344–48.
15. G.M. Swallowe, J.E. Field, C.S. Rees, and A. Duckworth: *Acta Metall.*, 1989, vol. 37, pp. 961–67.
16. R. Chow, R. Blindt, R. Chivers, and M. Povey: *Ultrasonics*, 2003, vol. 41, pp. 595–604.
17. R. Chow, R. Blindt, A. Kamp, P. Grocutt, and R. Chivers: *Ultrason. Sonochem.*, 2004, vol. 11, pp. 245–50.
18. R.M. Wagterveld, L. Boels, M.J. Mayer, and G.J. Witkamp: *Ultrason. Sonochem.*, 2011, vol. 18, pp. 216–25.

19. B.W. Zeiger and K.S. Suslick: *J. Am. Chem. Soc.*, 2011, vol. 133, pp. 14530–33.
20. R. Pecha and B. Gompf: *Phys. Rev. Lett.*, 2000, vol. 84, pp. 1328–30.
21. K.S. Suslick: *Encyclopedia of Physical Science and Technology*, Academic Press Inc., San Diego, CA, 2001, pp. 363–76.
22. J. Campbell: *Int. Met. Rev.*, 1981, vol. 26, pp. 71–108.
23. A. Hellawell, S. Liu, and S.Z. Lu: *JOM*, 1997, vol. 49, pp. 18–20.
24. D. Ruvalcaba, R.H. Mathiesen, D.G. Eskin, L. Arnberg, and L. Katgerman: *Acta Mater.*, 2007, vol. 55, pp. 4287–92.
25. A. Ludwig and W. Kurz: *Acta Mater.*, 1996, vol. 44, pp. 3643–54.
26. P. Tin, D. Frate, and H.C. de Groh, III: *Int. J. Thermophys.*, 2001, vol. 22, pp. 557–68.
27. M. Serefoglu and R.E. Napolitano: *Acta Mater.*, 2008, vol. 56, pp. 3862–73.
28. J. Klima, A. Frias-Ferrer, J. Gonzalez-Garcia, J. Ludvik, V. Saez, and J. Iniesta: *Ultrason. Sonochem.*, 2007, vol. 14, pp. 19–28.
29. F.R. Gilmore: *Hydrodynamics Laboratory Report 26-4*, California Institute of Technology, Pasadena, CA, 1952.
30. V. Minsier and J. Proost: *Ultrason. Sonochem.*, 2008, vol. 15, pp. 598–604.
31. Y. Lee, S. Karng, J. Jeon, and H. Kwak: *J. Phys. Soc. Jap.*, 1997, vol. 66, pp. 2537–40.
32. J. Holzfuss: *Phys. Rev. Lett.*, 1998, vol. 81, pp. 5434–37.
33. J. Pilling and A. Hellawell: *Metall. Mater. Trans. A*, 1996, vol. 27A, pp. 229–32.
34. A. Vogel, R.D. Doherty, and B. Cantor: *Solidification and Casting of Metals*, TMS, London, U.K., 1979, pp. 518–25.